Chapter 3

Ballistic and Coherent effects in InGaAs quantum dots

On fait la science avec des faits, comme on fait une maison avec des pierres : mais une accumulation de faits n'est pas plus une science qu'un tas de pierres n'est une maison

Henri Poincaré

3.1 Introduction

In this chapter, we investigate ballistic electron dynamics and electron coherence in QDs fabricated from InGaAs heterostructures. SEM micrographs of our QDs, labeled A_{1-3} and B_{1-3} (for samples prepared from wafer A and B, respectively), are shown in Fig. 3.1.

Previous works on open semiconductor QDs almost exclusively treated relatively large GaAs/AlGaAs QDs, with a small number of quantum channels in the leads. Our initial aim was to provide experimental data for smaller ballistic QDs, made from different materials, and compare to previous results in GaAs/AlGaAs QDs. InGaAs heterostructures were good candidate substrates in view of this purpose. As explained in previous chapter, the electron effective mass in InGaAs/InAlAs is significantly lower than in GaAs/AlGaAs heterostructures. Furthermore, structures with a higher 2DEG electron density, equivalent to a smaller λ_F, can be produced. Hence, our work complements existing data: as an example, we probe the regime

$\Delta \gg kT$, much more difficult to reach in GaAs/AlGaAs QDs, and we measured QDs with a large number of modes in the openings.

At first (section 3.2), we illustrate the basic phenomenology of magnetoconductance fluctuations and oscillations in our QDs. As explained in chapter 1, when the mean free path becomes larger than lateral dimensions of the QD, electrons can be viewed semiclassically as billiard balls. Depending on the geometrical symmetries of the QD, they can either follow stable periodic orbits, or probe particular trajectories between the entrance and exit point contacts, or be reflected back into the entrance point contact. In section 3.3, we analyze these classical ballistic effects in sample B_1, and show that they persist up to strikingly high temperatures.

Then, we focus on the extraction of the coherence time from the universal conductance fluctuations (section 3.4). We present and compare the methods used to obtain the temperature dependence of the coherence time in our samples, and analyze our results in light of existing theories in section 3.5. Finally, we investigate on the unexpected low-temperature saturation of the coherence time, observed in all of our QDs. Putting together our data with previous measurements on QDs, we propose a solution to this puzzling enigma (section 3.6).

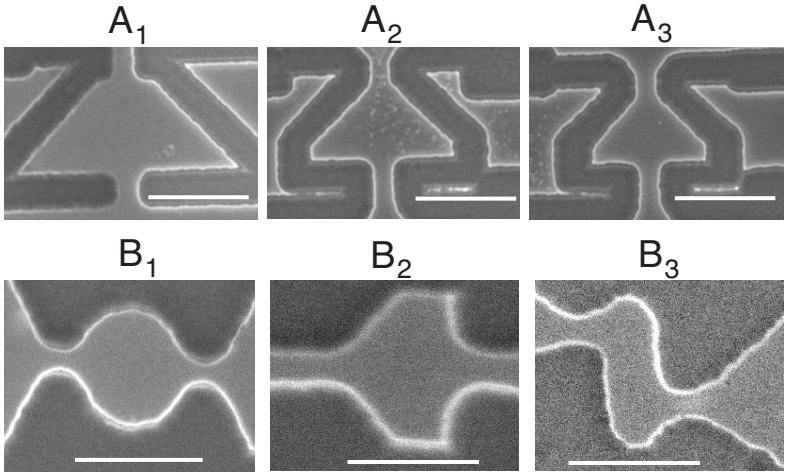

Figure 3.1: SEM micrographs of InGaAs QDs A_{1-3} and B_{1-3}. The white bar represents 500 nm.

3.2 Magnetoconductance

As the magnetic field is swept, changes occur in the electron dynamics inside the QDs. Different magnetic field regimes of transport in the QDs can be defined, as illustrated on Fig. 3.2, showing the magnetoconductance of samples A_1 and A_3 at 1.7 K along with the limits of these regimes for each QD. We first describe the *qualitative* features of each regime. A quantitative analysis of the magnetoconductance features in different regimes is proposed in the next sections.

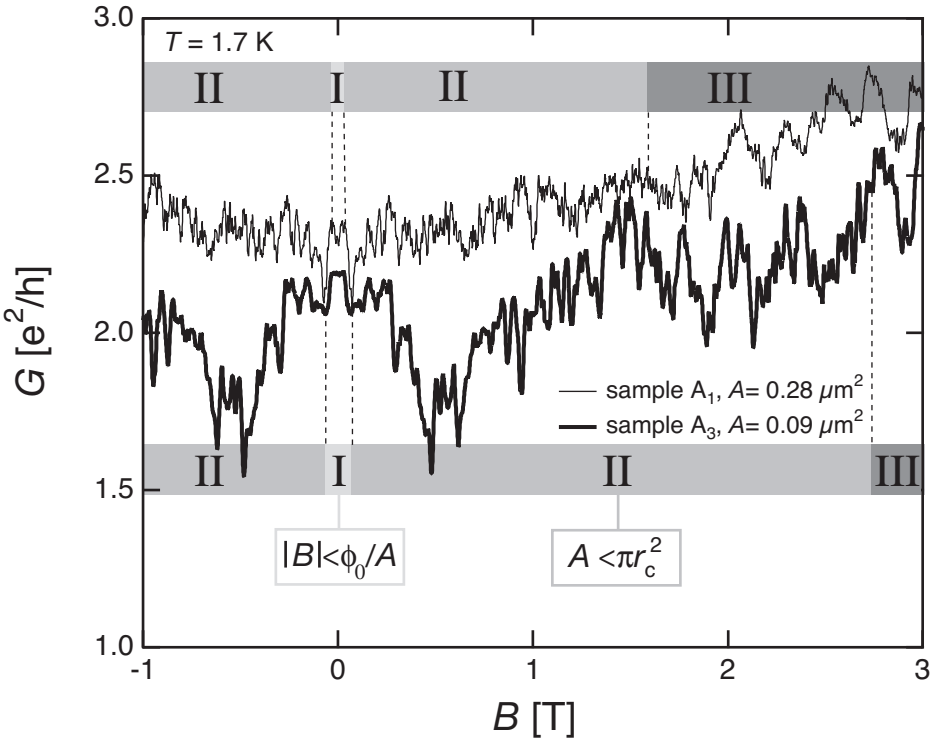

Figure 3.2: Magnetoconductance regimes in samples A_1 and A_3. The magnetoconductance of sample has been offset by 0.1 e^2/h.

In the low-$|B|$ regime (region I on Fig. 3.2), the trajectories can be approximated as straight lines, as the magnetic field has a negligible effect on the curvature of electron trajectories. Moreover, time-reversal symmetry holds, which means that coherent backscattering can occur (weak localization regime, see section 1.1.5). The magnetic field also induces phase

differences between the trajectories, giving rise to UCFs (see section 1.1.5). In our QDs, the weak localization-related enhancement of resistance around $B = 0$ is 'mixed' with UCFs. This means that, although there is always an extremum in G vs B at $B = 0$ (due to symmetry conditions), averaging over, *e.g.*, several QD shapes would be needed to evidence the WL effect. Region I is defined by the condition $|B| < \phi_0/A$, since, as $|B|$ is increased above ϕ_0/A, time-reversal symmetry is broken (one flux quantum penetrates the quantum dot).

At higher $|B|$, region II on Fig. 3.2, the curvature of electron trajectories becomes significant. In this regime, the semiclassical theory of transport still holds. Note that the typical B-scale of the fluctuations is larger in the QD with the smallest area (this will be detailed in section 3.4.2). This is in agreement with the semiclassical prediction for the conductance correlation function [92] [Eq. (1.9)]. When $|B|$ further increases, the cyclotron radius r_c becomes small enough that a cyclotron orbit can fit inside the billiard. This regime (region III) is known as the 'skipping orbit' regime, as the main trajectories contributing to the electron transport follow the edges of the cavity. Again, the onset of this regime depends on the size of the cavity. It corresponds to the condition $\pi r_c^2 = A$, where r_c is given by Eq. (1.3).

Notice also that the amplitude of the fluctuations is larger in the smallest QD (A_3) over the whole B-range, while their average conductance is very similar. The reason is explained in section 3.4.1.

Beside the different B-regimes, the QD magnetoconductance also strongly depends on temperature. We introduce the different temperature regimes by examining the magnetoconductance G vs B of sample B_1 over a wide T-range (from 1.3 up to 204 K). The magnetoconductance traces in Fig. 3.3 show the superposition of low-temperature fluctuations and broader oscillations (or 'peaks') with different temperature dependences, both symetric with respect to $B = 0$.

Low-temperature fluctuations are related to electron interference phenomena occuring inside the dot. The characteristic magnetic field scale is $\sim$ 0.01 to 0.1 T. They persist up to 30 K, much higher than in previous experiments on open QDs fabricated from AlGaAs/GaAs heterostructure [112, 86, 84]. The amplitude of the 'broader' oscillations decreases even slowlier, as they are still visible at 204 K, our highest measurement temperature. Their characteristic magnetic field scale is $\sim$ 0.5 T.

In summary, we define two temperature regimes: the high-T regime (where only broad oscillations are visible in the magnetoconductance) and the low-T regime (where broad oscillations and interference-related fluctuations contribute to the magnetoconductance). High-T oscillations are ana-

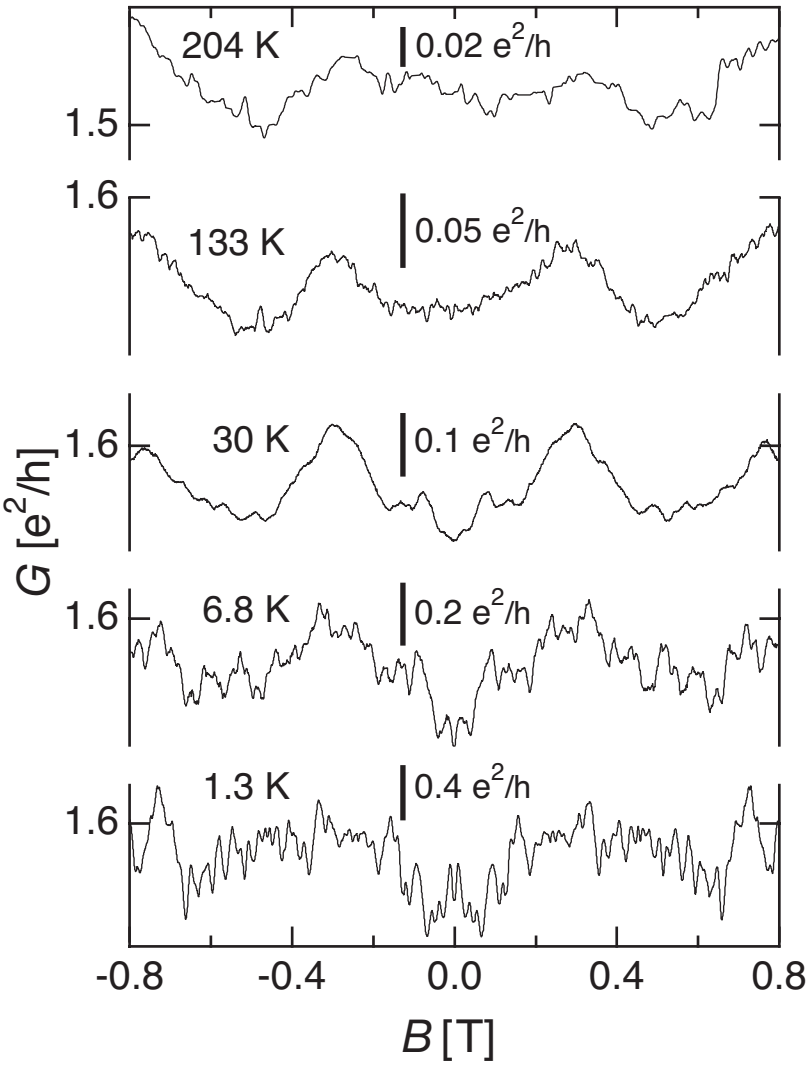

Figure 3.3: Magnetoconductance of sample B_1 at indicated temperatures. Notice the different conductance scales on top of each trace. The top gate is grounded for these measurements.

lyzed in the next section and low-T fluctuations are discussed in section 3.4.

3.3 High-T oscillations: focusing trajectories

At first, we analyze the high temperature G vs B data (in sample B_1). We will show that the broad magnetoconductance oscillations in this regime can be attributed to ballistic focusing effects.

Using the cyclotron radius formula [Eq. (1.3)] and given the size of the cavity, the magnetic field position of the expected semiclassical trajectories in the QD can easily be evaluated [106]. Fig. 3.4 shows that two trajectories linking both point contacts correspond to maxima of G vs B at 0.81 T and 1.47 T, and the minimum at 0.49 T is associated with an electron trajectory reflecting electrons in the origin point contact. The error bars on the graph take into account the uncertainty about the electron density and the depletion length.

We have assumed only one direction for carrier injection inside the cavity. A more realistic picture would take into account an injection cone, which effectively widens the peaks. These maxima and minima are robust with respect to small changes of the gate voltage V_g, as shown on Fig. 3.4. [1] This confirms that these oscillations are very different from UCFs, which are much more sensitive to small changes of E_F [21].

Following simple geometrical arguments, one could draw several other electron paths in the investigated magnetic field range, which should give rise to other minima and maxima in the magnetoconductance. However, all trajectories do not contribute equally to the magnetoconductance. As device boundaries are not perfectly shaped, electron reflections are not always specular. Therefore, trajectories involving a small number of such reflections have a larger contribution than more complicated paths. Moreover, the 'robustness' of classical trajectories with respect to changes of the injection angle is not constant among the trajectories, as shown, *e.g.*, in Ref. [109].[2]

The amplitude A_p of the peaks in G vs B, shown on Fig. 3.5(a) as a function of the temperature, are obtained after subtracting from each value of G vs B the value of the conductance linearly interpolated between each side of the peak (peak 1 is at $B = 0.81$ T and peak 2 is at $B = 1.47$ T). As this method adds the amplitude of a maximum to that of the adjacent

[1] We checked that, over the investigated V_g range, the change in n_s was too small to induce significant changes of the cyclotron radius.

[2] A very complete analysis of the stability of electron trajectories in triangular QDs is given in Ref. [106].

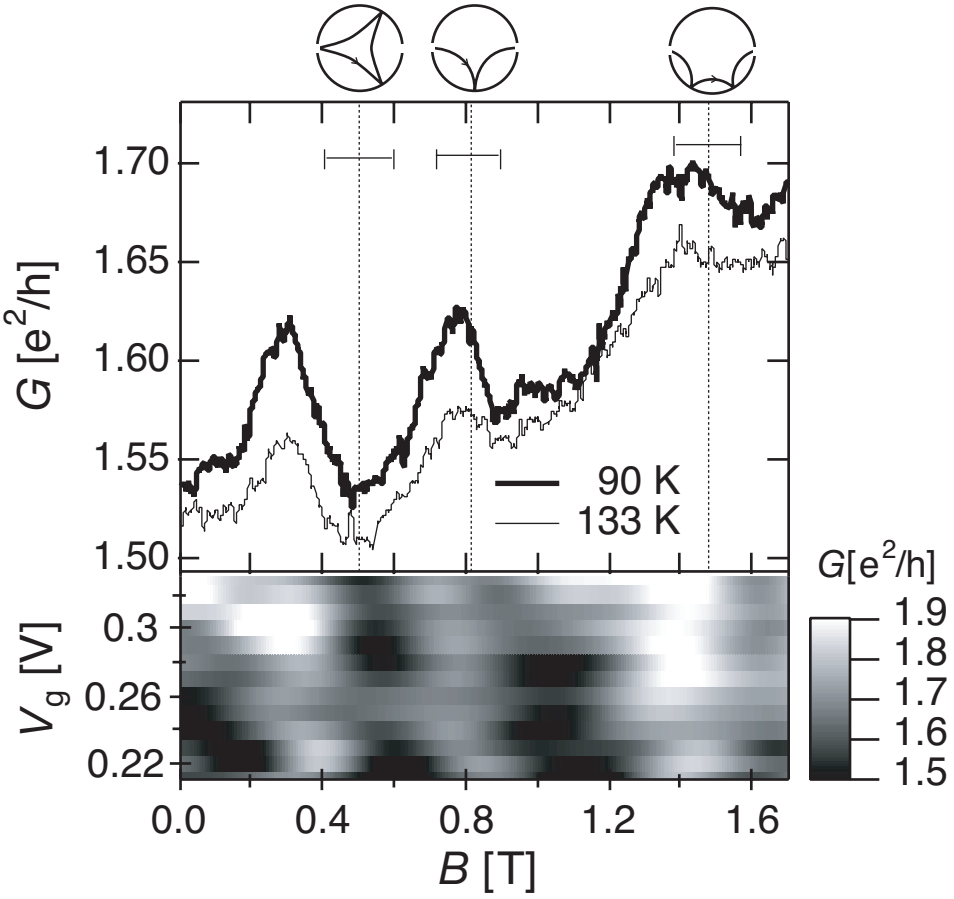

Figure 3.4: *top*: G vs B at high temperature in B_1, with positions of classical trajectories inside the cavity. *bottom*: colorplot of G as a function of B and V_g at low temperature. This colorplot is obtained from low-pass filtered G vs B traces with a cut-off frequency $3\mathrm{T}^{-1}$.

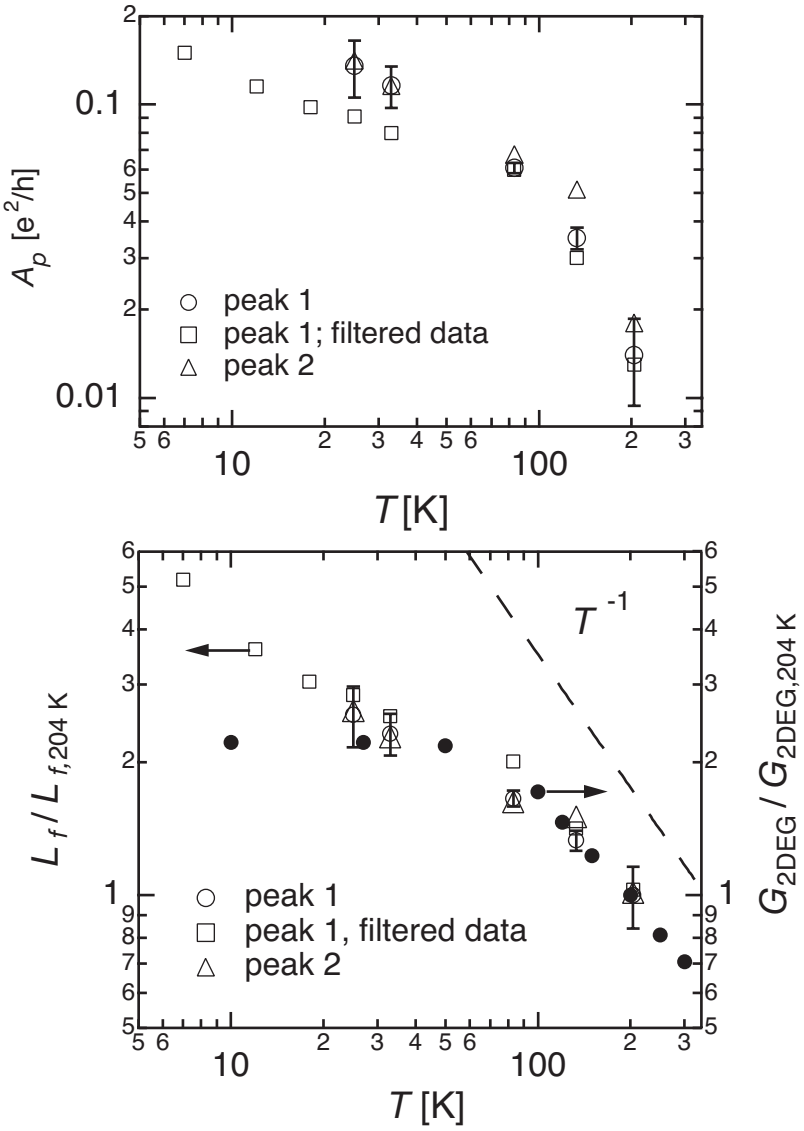

Figure 3.5: (a) Temperature dependence of the amplitude of peaks 1 and 2 (see text) in sample B_1. Open squares correspond to data extracted from low-pass filtered G vs B curves. (b) Temperature dependence of the change in L_f (open symbols) and in the longitudinal conductance of the 2DEG (filled symbols), both normalized to the value at 204 K. The dashed line represents a T^{-1} law.

minima, it only gives an indication on the temperature dependence of A_p, but not on the absolute value. Note also that the extraction of A_p was limited to above 20 K, because UCFs amplitude becomes comparable to the amplitude of the oscillations. To overcome this limitation, we have also extracted A_p from low-pass filtered G vs B curves below 20 K. A_p vs T (Fig. 3.5(a)) show no saturation at low temperature, which is reminiscent of the temperature dependence of the magnetoconductance peaks observed in focusing experiments.

Focusing measurements [151, 75, 73] evidenced that the focusing peak amplitude A_p depends on the trajectory length L_e and the 'focusing mean free path' L_f according to Eq. (1.4) (section 1.1.3). The maxima at $B = 0.81$ T (peak 1) and 1.47 T (peak 2) correspond respectively to trajectory lengths $L_e \sim 596$ nm and 700 nm, both larger than the electron mean free path in this QD, even at low temperature. This confirms that ballistic effects can still be observed when $L_e \gtrsim l_\mu$, as already evidenced by Hirayama and Tarucha [78].

In order to calculate L_f from Eq. (1.4), the value of A_0 has to be determined. This requires a reference value for L_f at a given temperature, which is not available. Therefore, we only calculate the change in L_f with respect to its value at 204K, $L_f/L_{f,204\mathrm{K}}$. Fig. 3.5(b) compares these data to the relative change in the longitudinal conductance of the unpatterned two-dimensional electron gas, $G_{2\mathrm{DEG}}$, with respect to the conductance at 204K, $G_{2\mathrm{DEG},204\mathrm{K}}$. $G_{2\mathrm{DEG}}/G_{2\mathrm{DEG},204\mathrm{K}}$ is directly proportional to the mean free path l_μ.

We observe a clear saturation of $G_{2\mathrm{DEG}}/G_{2\mathrm{DEG},204\mathrm{K}}$ below $\sim$50 K, while, as T decreases, $L_f/L_{f,204\mathrm{K}}$ increases continuously. This difference likely comes from a different sensitivity of l_μ and L_f to small-angle scattering mechanisms, as already evidenced by Heremans and co-workers in different types of focusing experiments [73, 72]. At low temperature, while L_f is influenced both by small-angle electron-phonon scattering *and* elastic scattering, l_μ is only affected by the latter mechanism (this implies $L_f < l_\mu$ [75]). On the contrary, in the high-temperature limit, the temperature dependences of $G_{2\mathrm{DEG}}/G_{2\mathrm{DEG},204\mathrm{K}}$ and $L_f/L_{f,204\mathrm{K}}$ are similar, which means that both l_μ and L_f are governed by the same mechanisms: electron-phonon scattering. As the above analysis reveals that the temperature dependence of L_f in our QDs is very similar to results obtained in pure focusing experiments, we associate high-T oscillations to focusing trajectories.

Performing a similar analysis on data from the other open quantum dots is not as straightforward as for B_1. The reason is that the geometrical symmetry of the other QDs is lower. As B_1 is (almost) circular, it possesses

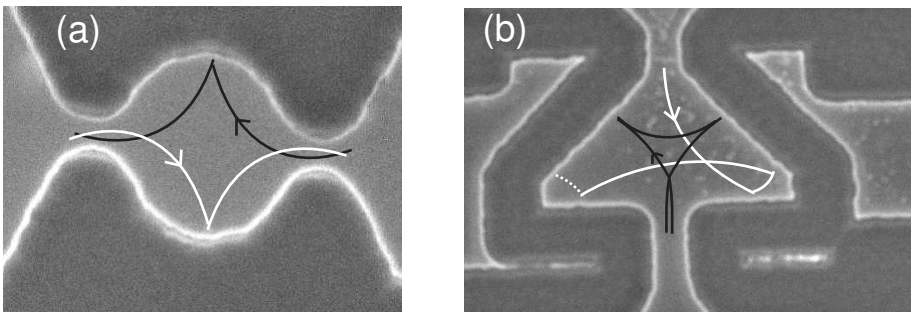

Figure 3.6: (a) Two classical trajectories for electrons injected from the left (in white) or right (in black) QPC in sample B_1. (b) Two classical trajectories for electrons injected from the top (in white) or bottom (in black) QPC in sample A_2.

symmetry axes both parallel and perpendicular to the current direction. Therefore, we expect that the sequences of scattering events of electrons injected from both openings are similar, as shown on Fig. 3.6(a).

Conversely, when there is no symmetry axes perpendicular to the current flow, as in all the other QDs, this no longer holds: even if, for a particular B, electrons injected from one of the openings follow an 'easy' trajectory to the other opening, it is not likely to be true for electrons injected from the other opening. This is illustrated on Fig. 3.6(b) in the case of sample A_2.

In our conductance measurements, the current is injected from both openings since we use an ac lock-in technique. As a result, the effect of periodic orbits or stable trajectories on the magnetoconductance is somewhat averaged out in asymmetric devices. However, there is still a high-temperature background in the G vs B curves of the other (asymmetric) QDs, but it is much more difficult to associate maxima and minima in this background to periodic classical orbits.

3.4 Low-T fluctuations : τ_ϕ extraction

The analysis of UCFs in the low-T regime enables us to extract the phase coherence time τ_ϕ. In most previous experiments [86, 84, 130], the determination of τ_ϕ in QDs was based on the measurement of the weak localization peak height or width, after averaging over a large number of magnetoconductance traces corresponding to different dot shapes (but with the same

area), in order to reduce UCFs amplitude (Fig. 1.8, and section 1.1.5).

In our samples, the geometry of the QDs is not defined by metalic gates, but rather by wet etching. In some QDs (B_{1-2}), a gate is deposited over the whole structure. In this case, the gate voltage V_g not only changes the shape of the QD, but also its area, and the electron density. This makes the weak localization method impossible to apply in our QDs, and forces us to look for alternative methods.[3]

Since we are interested in the determination of the absolute value of τ_ϕ, and not just its temperature dependence, we consolidate our data analysis by the use of two different methods to extract τ_ϕ from UCFs. The first one (presented in the next section) is based on the measurement of UCFs variance at low magnetic field, which was shown to be equivalent to the weak localization method [85]. The second method, presented in section 3.4.2 is based on the autocorrelation field of the UCFs at high magnetic field.

3.4.1 Low-B UCFs (RMT)

Random Matrix Theory provides several formulas relating $var(G)$ and τ_ϕ (section 1.2.4). The first step in our analysis is therefore to obtain $var(G)$. This requires to separate "electron-interferences-related" fluctuations from the slowly varying background of ballistic oscillations discussed in the previous section. In order to identify the contribution of these slow oscillations to G vs B, we compare the power spectrum (PS) of G vs B at low temperature (2.3 K) and at high temperature (83 K), where UCFs have disappeared (Fig. 3.7(a), sample B_1).[4] At low frequencies ($\lesssim 2$ T^{-1}), the PS is clearly temperature-independent, while it strongly depends on T at higher frequencies ($\gtrsim 2$ T^{-1}). Based on this observation, we evaluate $var(G)$ from high-pass filtered G vs B traces, with a cut-off frequency $f_c = 2 - 3$ T^{-1} (depending on the sample - the error bar over τ_ϕ takes into account this uncertainty). Such a filtering procedure also removes a small contribution of low-f UCFs from $var(G)$. This is a cause of a slight underestimation of τ_ϕ.

Fig. 3.7(b) shows that $var(G)$ follows a $\sim T^{-1.5}$ law in B_1. The error bar over $var(G)$ grows with T, as $var(G)$ becomes comparable to the amplitude

[3] Note also that at high absolute voltage, we measured a leakage current between the 2DEG and the gate. In this regime, it is no longer possible to perform reliable measurements of G. This prevented the use of top gates to completely deplete the 2DEG underneath (and, hence, to fabricate top-gate-defined QDs).

[4] Spectra in Fig. 3.7(a) are averages of 3 fast Fourier transforms power spectra from half overlapping blocks in the range 0.3 T $< B <$ 4 T.

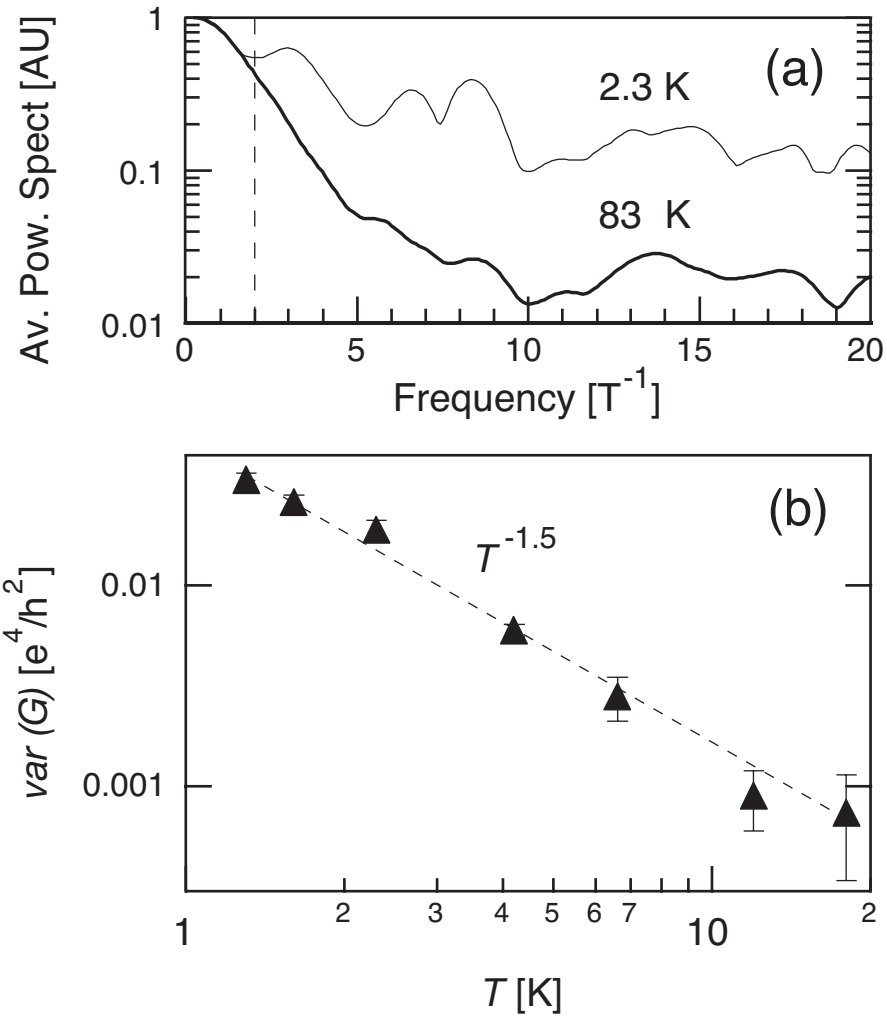

Figure 3.7: (a) Average power spectrum of conductance fluctuations at 2.3 and 83 K in B_1, in arbitrary units. The dashed line corresponds to the cut-off frequency f_c (see text). (b) $var(G)$ as a function of T, in units of e^4/h^2, evaluated in the range $0.3T < B < 1T$. The dashed line is a fit to a $T^{-1.5}$ law.

of the slowly varying background at 20 K. Note that $var(G)$ is evaluated in the range 0.3 T $< B <$ 1 T, so that r_c is larger than the cavity radius, and time-reversal symmetry is broken (regime II on Fig. 3.2).

Next, we have to choose the adequate expression to evaluate τ_ϕ from $var(G)$. In a previous work [85], an approximated expression was used, strictly valid if $\Delta \ll kT$. This condition is not fulfilled in our samples at low temperature, due to the large value of Δ. Therefore, we have to use the following generalized formula for the variance of UCFs, including dephasing and thermal averaging [57]:

$$var(G) = \int_0^\infty \int_0^\infty f'(E) f'(E') cov(E, E') dE dE', \tag{3.1}$$

where E and E' are energies, $f'(E)$ is the derivative of the Fermi function and $cov(E, E')$ is the conductance correlator. Here, we use:[5]

$$cov(E, E') = \frac{\langle G \rangle^2}{(N + N_\phi)^2 + 4\pi^2 (E - E')^2 / \Delta^2}. \tag{3.2}$$

This correlator is equivalent to Eq. (14) of Ref. [28], with $a = b = 0$ (spinless case), and $\langle G \rangle$ given by Eq. (13) of Ref. [28], which depends on N_1, N_2 (the number of modes in each QPC) and N. As indicated by the authors, Eq. (13) and (14) of Ref. [28] with $a = b = 0$ recover the result of Frahm [57], and is equivalent to the 'universal' behavior for $var(G)$ predicted by RMT in the case of $T \to 0$ and $N_\phi \to 0$ [17, 94]. The total number of modes N in the leads is determined from the average conductance of the QD, according to Eq. (1.14).[6] In the case of non-integer average conductance, we assume that the number of modes is not equal in both QPCs: *e.g.* in B_1, the average conductance is 1.4 e^2/h, so that $N = 3$, the two QPCs supporting respectively one and two quantum modes.

Equations (3.1) and (3.2) explain the different amplitudes of UCFs in samples A_1 and A_3, observed on Fig. 3.2. Samples A_1 and A_3 have similar $\langle G \rangle$, N and τ_ϕ, but, as A is larger in A_1, Δ is smaller, so that $cov(E, E')$ and hence $var(G)$ are smaller in A_1.

[5] In the next chapter concerning bismuth systems, we use two additional correlators, due to the contribution of SO coupling and imperfect leads.

[6] This means that we assume that the measured QD conductance is dominated by the point contact contributions, which are taken to add as Ohmic resistors in series for the determination of the number of modes [see Eq. (1.14); in this chapter, N is the total number of modes in the QPCs, while M in Eq. (1.14) is the number of modes in each QPC]. This also implies that the transmission factor through the QD is large (close to 1).

Eq. (3.1) is solved numerically to extract τ_ϕ. Note that using this method in the case of a small N_ϕ (large τ_ϕ) with respect to N may yield very large uncertainty over τ_ϕ. This is the source of a significant contribution to the error bar over τ_ϕ in the case of sample B_1 (see below), and also prevents any reliable extraction of τ_ϕ in B_2 using this method (*i.e.* the error bar would be prohibitively large in the case of this sample).

3.4.2 High-B UCFs

The second method to extract τ_ϕ is based on the high-B dependence of the UCFs, as already used for QDs in Refs. [23, 130] and for wires in Ref. [29]. This method is not based on the amplitude of the fluctuations, but rather on their typical 'period', or typical B-scale.

Fig. 3.8(a) shows the magnetoconductance of sample A_1 at 1.7 K. At first sight, one can see that the typical B-scale of the fluctuations is larger at high-B than at low-B. This is related to the formation of skipping orbits at the edge of the cavity, as the cyclotron orbit size becomes smaller than the QD dimension [this happens for $B \gtrsim 1.6$ T in A_1, as indicated by the dashed line on Fig.3.8(a)]. In this regime, the effective area for electron interferences (enclosed between the skipping trajectories and the QD edges) decreases as B increases. This causes the broadening of the B-scale of the fluctuations.

To be more quantitative, we formalize this simple picture. At first, we define the correlation function (see also section 1.2.3):

$$C(\Delta B) = \langle [G(B) - \langle G(B) \rangle][G(B + \Delta B) - \langle G(B) \rangle] \rangle. \qquad (3.3)$$

In Fig. 3.8(b), we show two normalized correlation functions, calculated over different B-ranges (at low-B and high-B) using Eq. (3.3). The correlation field B_c (the "typical B-scale of the fluctuations") is then defined from the half-width of this correlation function : $F(B_c) = F(0)/2$. It is clear from Fig. 3.8(b) that B_c is larger for the high B correlation function. B_c calculated using this method is shown on Fig. 3.8(c) as a function of the mean B value in each range. In the 'skipping orbit' regime, B_c vs B linearly increases, due to the shrinking of the area for electron interferences as B increases. It can be demonstrated that B_c vs B is directly related to τ_ϕ [23]:

$$B_c(B) = 8\pi^2 m^* B / h k_F^2 \tau_\phi + C, \qquad (3.4)$$

where C is a constant.[7] We directly obtain τ_ϕ by fitting B_c vs B with Eq. (3.4). As an example, the fit on Fig. 3.8(c) gives $\tau_\phi \sim 2 \pm 0.3$ ps.

[7] This constant has been added to account for the fact that $B_c(B = 0)$ cannot be equal

It is important to note that when the amplitude of Shubnikov-de Haas oscillations becomes significant compared to UCFs amplitude, this method can no longer be used. This condition hence defines the upper limit in magnetic field of the range where this method is applicable. In some samples, this range is so reduced that no reliable result could be obtained using this method. This point is particularly critical in small-area QDs, with small UCFs amplitude, such as A_3. In this case, Shubnikov-de Haas oscillations may be non-negligible at the onset of the skipping-orbit regime.

3.4.3 Comparison of τ_ϕ extraction techniques

In our samples, the temperature dependence of τ_ϕ was exclusively obtained using the two methods detailed in previous sections, namely the RMT method and the correlation field method. In two samples (A_1 and B_1), both techniques could be used.

Fig. 3.9 shows the comparison between the values of τ_ϕ obtained with both methods in the latter samples. [8] The error bars on τ_ϕ take into account the uncertainty about $var(G)$ (due to the choice of the cut-off frequency), N, T, Δ and $\langle G \rangle$ in the case of RMT method, and, in the case of the correlation field method, the uncertainty about the linear fit of B_c vs B (which is by far the main contribution to the error bar over τ_ϕ). The overall agreement between the methods is reasonable, knowing that their foundations are different. This agreement indicates that our data are not significantly affected by the limitations of the RMT in the case of QDs with non-ideal QPCs [11]: as already pointed out in section 1.2.4, this type of correction is small when $N_\phi \gg 1$, a condition which is satisfied in our samples. However, we observe on Fig. 3.9 that the correlation field method always yields smaller values for τ_ϕ (factor of 1.5 - 2 reduction with respect to RMT results). This discrepancy may come from the different electron dynamics inside the QDs in different magnetic field regimes.

In the other QDs, only one method could be applied to extract τ_ϕ. In B_2, the RMT method yielded a very large uncertainty on τ_ϕ over the whole temperature range, so we only used the correlation field technique to determine τ_ϕ [9] (this was only possible for one temperature, for which we measured G

to zero (this is confirmed experimentally on Fig. 3.8(c), and in previous experimental works [23]). However, there is no theoretical background to support it.

[8] Concerning τ_ϕ vs T in B_1, Fig. 3.9 displays results extracted using parameters slightly different from those used in ref. [64]. This is the origin of the small difference with τ_ϕ vs T data that we published in Ref. [64].

[9] Note that $var(G)$ vs T data for this sample is available and is presented below.

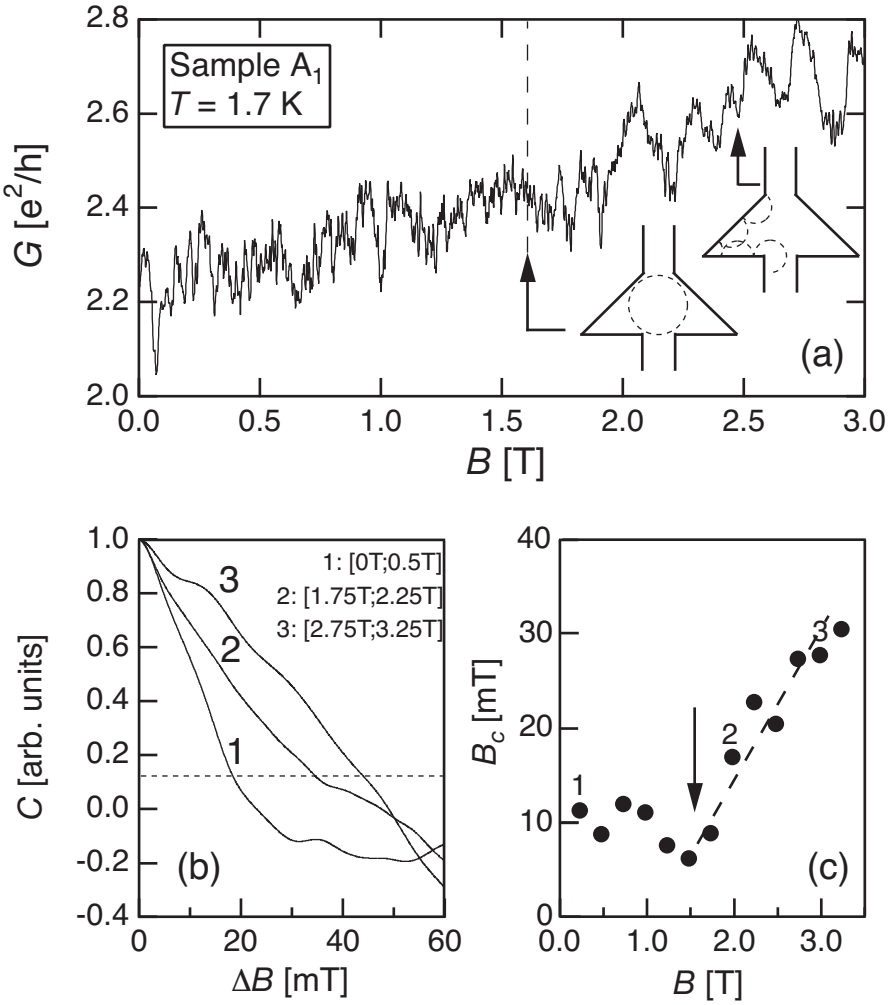

Figure 3.8: (a) Magnetoconductance of sample A_1 at 1.7 K. The dashed line marks the transition to the "skipping-orbits" regime. (b) Correlation function F vs ΔB calculated over the indicated magnetic field ranges (F is normalized at 1 for $\Delta B = 0$). The curves are obtained after averaging over five correlation functions calculated on smaller ranges. (c) Correlation field B_c vs B. The dashed line is a linear fit to the data in the skipping orbits regime (the onset of this regime is indicated by the arrow).

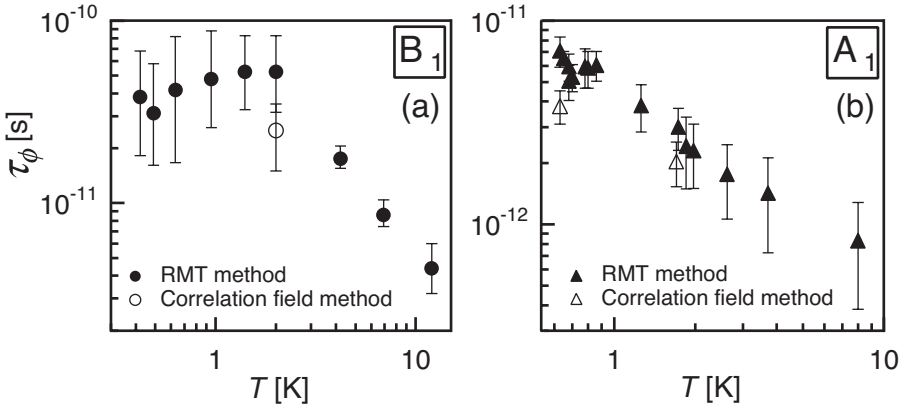

Figure 3.9: (a-b) τ_ϕ vs T in samples B_1 and A_1 obtained using the RMT method (filled symbols) and the correlation field method (open symbols).

vs B at sufficiently high B). For the remaining samples (A_2, A_3 and B_3) we used exclusively the RMT method, either due to the lack of measurements at sufficiently high B, or to the too reduced B-range of applicability of the correlation field method (see above).

3.5 Temperature dependence of τ_ϕ

After the presentation of the extraction methods, we examine the extracted data. First, we concentrate on τ_ϕ vs T data from sample B_1, shown on Fig. 3.10 (filled circles) along with data from B_2 and B_3. We clearly observe two temperature regimes, with distinct T-dependences of τ_ϕ: the low-temperature regime is characterized by a very weak or an absence of temperature dependence (saturated regime), while the T-dependence is much stronger in the high temperature regime. As we show below, all our InGaAs QDs show a similar behaviour.[10]

To begin, we consider only the high temperature regime. The bold line on Fig. 3.10 is the theoretical prediction for e-e scattering in a diffusive 2D system with the parameters of wafer B, *i.e.* Eq. (1.22) with $E_F = \frac{\hbar^2 \pi n_s}{m^*} = 55.3$ meV, $l_\mu = 500$ nm and $\lambda_F = 16$ nm. Note that Eq. (1.22) does not have any adjustable parameters. Surprisingly, in B_1, we observe

[10]The transition temperature ($T_{\rm onset}$) between these regimes will be rigorously defined in the next section.

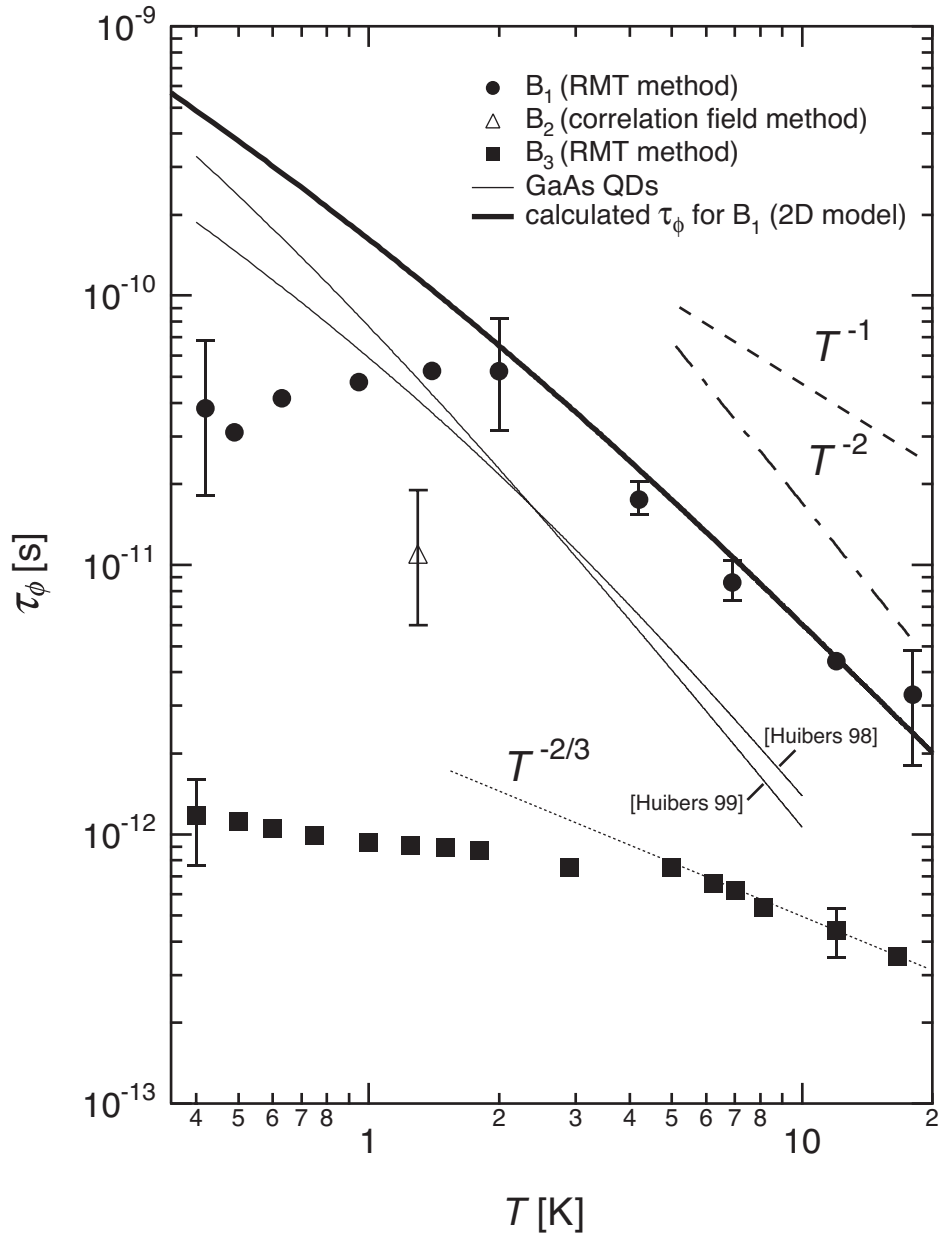

Figure 3.10: τ_ϕ vs T in B_{1-3}. Bold line: theoretical τ_ϕ vs T in sample B_1 [calculated using Eq. (1.22)]. Solid lines: τ_ϕ vs T in GaAs QDs (Refs. [86, 84]). The dashed line indicates T^{-1} law, dotted line indicates $T^{-2/3}$ law and dash-dotted line indicates T^{-2} law.

a remarkable quantitative agreement between the measured τ_ϕ vs T and this model in the high temperature range.[11] Hence, in B_1, decoherence is fully determined by '2D' e-e interactions, and electron-phonon scattering is negligible even at 20 K. We recall that, in 2D samples, a rate $\tau_\phi^{-1} \propto T^3$ is expected when electron-phonon interaction dominates [120].

Table 3.1: Summary of relevant transport parameters for B_1 and GaAs QDs, with the experimental fits to $\tau_\phi(T)$.

	B_1	GaAs[84]	GaAs[86]
$m^*(*m_0)$	0.04	0.067	0.067
$n_s(10^{15}\mathrm{m}^{-2})$	9.7	2	1.8
$l_\mu(\mathrm{nm})$	500	1500	6000
$A(\mu\mathrm{m}^2)$	0.113	$8-1.6$	$4-0.4$
$\Delta(\mu\mathrm{eV})$	90.6	$0.8-4$	$1.8-17.9$
$E_F(\mathrm{meV})$	55.5	7.15	6.44
λ_F/l_μ	0.05	0.037	0.01
$\tau_\phi^{-1}(\mathrm{ns}^{-1})$	$5(\pm2)T + 1.1(\pm0.3)T^2$	$4T + 9T^2$	$10.9T + 6.1T^2$

Fig. 3.10 also compares our data with the electron coherence time in GaAs quantum dots [86, 84].[12] The temperature dependence of τ_ϕ is clearly similar in B_1 and in GaAs QDs at high temperature. One can therefore reasonably conclude that, in the high-T regime, dephasing is governed by the same scattering mechanisms.

However, τ_ϕ is ~ 2 to 4 times larger in B_1 than in GaAs QDs at high temperature (non-saturated regime). In order to explain the origin of this larger τ_ϕ in B_1, we have gathered the main parameters of our sample in Table 3.1, along with the data on GaAs QDs from References [86, 84]. In the same way as Huibers and coworkers [86, 84], we performed a fit of the

[11] We recall that, even at 20 K, transport is still ballistic in B_1: the mean free path (500 nm) is almost constant up to 50 K in all our wafers (see Fig. 1.1), and is larger than the dimensions of the QD. Therefore, as B_1 does not fulfill the hypothesis of the model (1.22), it is surprising to observe such a good agreement between this theory and our experiment. We refer to section 1.3.2 for a discussion of the (few) available models for the T-dependence of τ_ϕ in 0D. These models do not fit to our data.

[12] The experimental fits for τ_ϕ vs T in GaAs/AlGaAs QDs (Fig. 3.10) are extrapolated up to 10 K for comparison purposes: the data were measured in the range $0.03\ \mathrm{K} < T < 4\ \mathrm{K}$.

form $\tau_\phi^{-1}(T) = aT + bT^2$ to our data, where a and b are constants (this is an approximated form of Eq. (1.22)). The coefficient of the T^2 term is a factor of 6 to 9 smaller in InGaAs QD than in GaAs/AlGaAs QDs, while the coefficient of the T term varies only by a factor of ~ 2 to 3 among the various samples. The difference in the coefficient of the T^2 term can be explained by the larger E_F in our sample [see Eq. (1.22)], originating from a smaller m^* and a larger n_s. This explains the larger value of τ_ϕ in B_1. Note that, around 1K, τ_ϕ in our InGaAs QD becomes closer to the τ_ϕ given in ref. [84]. In this range, τ_ϕ vs T is dominated by the T term, which depends on the ratio λ_F/l_μ. Table 3.1 clearly shows that this ratio in our sample is indeed very close to that in ref. [84].

Next, we examine the data for the other QDs. The only data point available for B_2 does not allow for much discussion. Nevertheless, we observe that τ_ϕ is lower than in B_1 at this temperature. As we will show below from $var(G)$ vs T data, τ_ϕ in B_2 is in the saturated regime at this temperature, so that we can not infer anything about its T-dependence in the high temperature regime.

The nice simple picture presented above for B_1 clearly breaks down in the case of sample B_3, fabricated on the same parent substrate as B_1, but with a larger n_s due to the illumination during sample cooldown ($n_s = 2.8 \times 10^{16}$ m^{-2} in B_3 compared to $n_s = 10^{16}$ m^{-2} in B_1). τ_ϕ has indeed a weaker T dependence ($\sim T^{-2/3}$) and a much smaller absolute value in B_3 than in B_1. Using the parameters of B_3, τ_ϕ predicted by Eq. (1.22) is ~ 1 to 2 orders of magnitude larger than experimental values in the high temperature (T-dependent) regime.

The reason for this discrepancy is most probably that the increased n_s causes the population of the second electronic subband, as shown by the beating pattern in the Shubnikov-de Haas (SdH) oscillations, measured close to the cavity B_3 (Fig. 3.11). From Hall measurements performed simultaneously with the UCFs measurements on the QD, we estimate $n_s \sim 2.8 \times 10^{16}$ m^{-2}. The total electron density obtained from SdH oscillations is a bit larger $\sim 3.4 \times 10^{16}$ m^{-2}. The origin of this enhancement is that the data were measured during different cooldowns of the sample (and most probably a different number of photo-generated carriers). SdH data also yield a sheet density 2.8×10^{16} m^{-2} for the first subband. It is therefore very likely that the onset of second subband population was reached during the UCFs measurements on B_3.

Second subband population affects the electron mobility, as reported in Ref. [150]. However, taking into account even a large change of mobility in

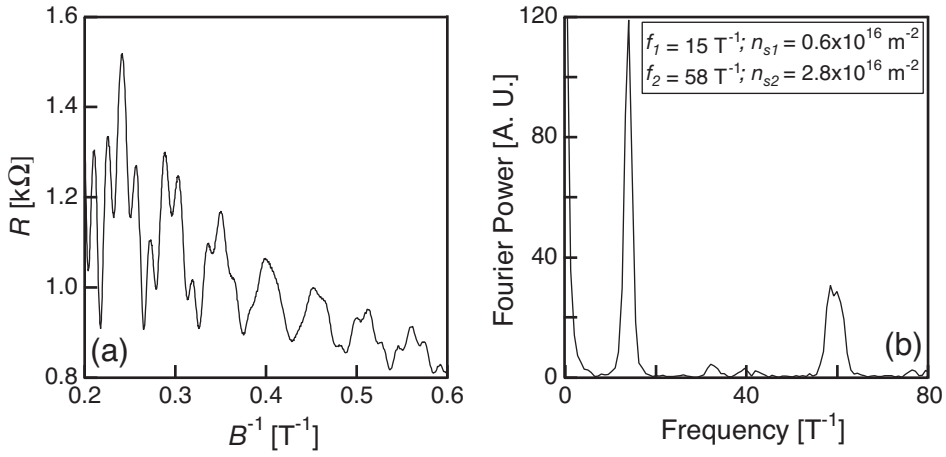

Figure 3.11: (a) Longitudinal resistance as a function of the inverse magnetic field at 0.3 K, measured close to the QD on sample B_3. Two distinct periods are observed in the Shubnikov-de Haas oscillations. (b) Fourier power (arbitrary units) vs frequency, calculated from the magnetoresistance data in (a). f_1 and f_2 are the frequencies corresponding to the main local maxima in the Fourier power spectrum. n_{s1} and n_{s2} are the electron sheet densities calculated from f_1 and f_2.

Eq. (1.22) would not reproduce our data. Therefore, we believe that the population of the second subband causes the emergence of an additional contribution to the electron decoherence rate in our QDs, larger than the contributions of Eq. (1.22), and characterized by $1/\tau_\phi \propto T^p$ with $p < 1$. A $T^{-0.8}$ dependence for τ_ϕ was recently reported by our group in a QD fabricated from a wide GaAs quantum well with two occupied subbands [63], which is in agreement with our hypothesis. Furthermore, a recent experiment on illuminated unpatterned 2DEGs fabricated from $In_{0.53}Ga_{0.47}As/InP$ heterostructures confirms that $1/\tau_\phi$ significantly increases when the second subband is populated [135]. As far as we know, a theory describing this increased decoherence rate in two-subband 2DEGs or QDs does not exist yet. However, decoherence rates are related to the number of available states, which means that the contribution of the states available in the second subband is likely to be the origin of the large decrease of τ_ϕ observed in our case.

Disagreement with the conventional 2D dephasing theory [Eq. (1.22)] is also observed in the remaining samples, fabricated from wafer A. τ_ϕ vs T data from these samples are shown in Fig. 3.12(e-g). While the observed

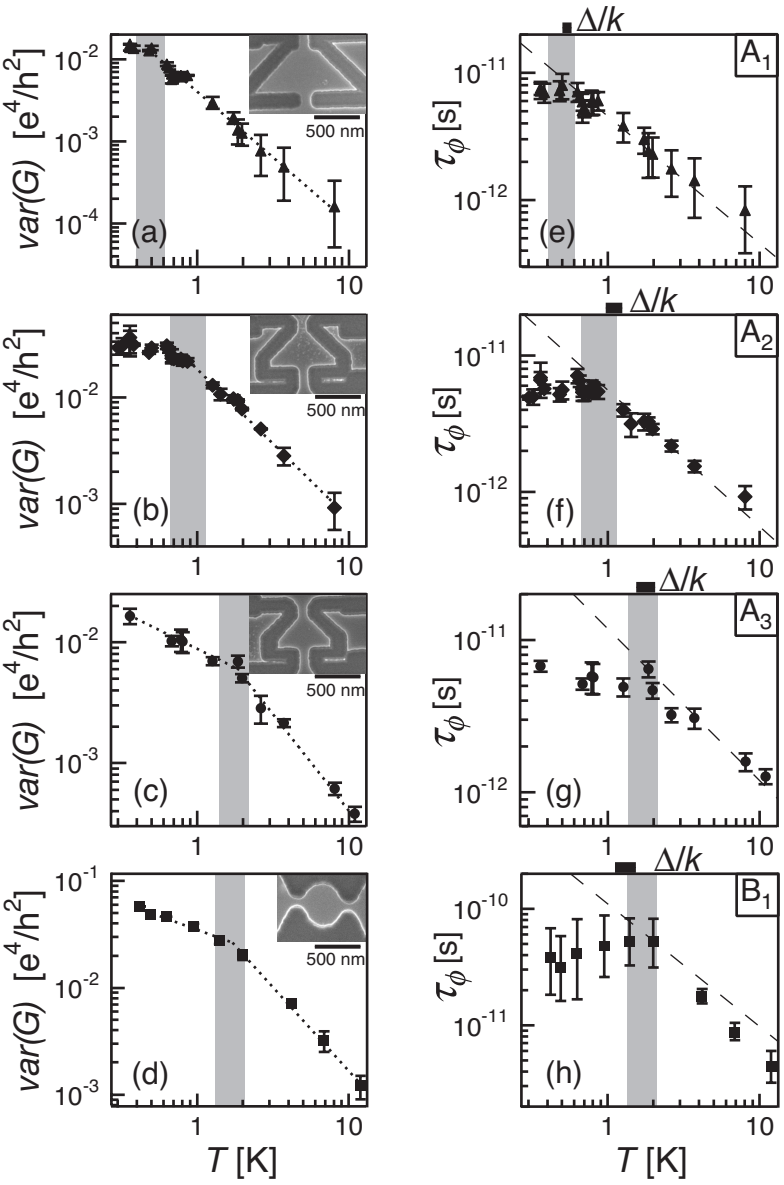

Figure 3.12: (a-d) $var(G)$ vs T in A_{1-3} and B_1. The shaded area corresponds to $T_{\rm onset}$ (with its error bar). Insets show micrographs of the samples (dark areas are etched). Dotted lines are fits to T^{-a} (with different a for each QD). (e-h) τ_ϕ vs T in A_{1-3} and B_1. Δ/k is indicated above each graph, with its error bar, as a black rectangle. Dashed lines correspond to $\tau_\phi \sim T^{-1}$ laws.

temperature dependence in these QDs ($\tau_\phi \sim T^{-1}$, in the high-T regime) is in agreement with Nyquist electron-electron scattering in 2D, a quantitative comparison with this model's prediction reveals a strong discrepancy: the theoretical values are about one order of magnitude larger than the experimental τ_ϕ. The electron density in A_{1-3} ($n_s = 2.4 \times 10^{16}\mathrm{m}^{-2}$) is slightly lower than in B_3. However, beating in the Shubnikov-de Haas pattern (if any) is much less clear in wafer A than in B_3. Nevertheless, Saveliev and coworkers [135] showed that the decoherence rate can be affected even by a very small electron concentration in the second subband.

To summarize, our data confirm the need for a more detailed microscopic theory of dephasing in 0D conductors, taking into account geometrical aspects as well as the contribution of intersubband scattering. Although τ_ϕ in B_1 is in good agreement with prediction of the existing theory for disordered 2D systems, decoherence rates are much larger than expected in A_{1-3} and B_3, probably due to second subband population (although no theory is available to check this hypothesis). Nevertheless, the T-dependence is not far from theoretical predictions for 2D disordered systems.[13] We can therefore not rule out that a theory more adapted to our particular situation (*i.e.* 0D ballistic systems), but without any contribution from intersubband scattering would explain our data.

3.6 Saturation of τ_ϕ

Here, we examine the low-temperature τ_ϕ vs T, where τ_ϕ is found to saturate, and focus on the onset of this regime. In order to identify possible origins of this saturation, we first investigate the effect of the QD area. With $\langle G \rangle$ close to e^2/h, both $var(G)$ and τ_ϕ data from A_{1-3} and B_1 are presented in Fig. 3.12. For each QD, two temperature ranges, with distinct temperature dependences, are clearly visible. In both ranges, $var(G)$ is fitted by a $\sim T^{-a}$ law, with a smaller a in the low-T range.[14] The crossing-point of the two power-law fits then defines the transition temperature T_{onset} between the two regimes. Fig. 3.12(a-d) shows T_{onset} with its error bar as a shaded area. Obviously, T_{onset}, which also corresponds to the onset for the saturation of τ_ϕ [15] (as shown on Fig. 3.12(e-h)), increases as the QD area decreases. Since experimental setup, $\langle G \rangle$ and heterostructures are essentially unchanged for

[13] $\tau_\phi \propto T^{-p}$, with an observed $1 \lesssim p \lesssim 1.5$ and $p \sim 2/3$ in a particular case, compared to a predicted $1 < p < 2$.

[14] Note that a depends on the sample parameters.

[15] T_{onset} is more precisely determined from $var(G)$ vs T than from τ_ϕ vs T: the relative error over τ_ϕ as well as the dispersion of τ_ϕ vs T data is larger than in the case of $var(G)$.

all 4 samples, this result clearly shows that the saturation is indeed intrinsic to the QDs and that the ruling physical parameter(s) need to be seeked.

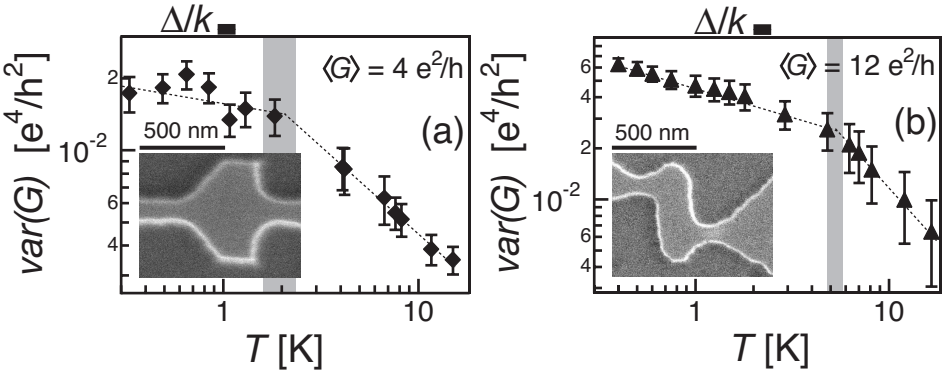

Figure 3.13: (a-b) $var(G)$ vs T in B_2 and B_3. Insets show micrographs of the samples. Dotted lines are fit to power laws. Δ/k is indicated above each graph, with its error bar, as a black rectangle.

More quantitatively, our data in Fig. 3.12 show that Δ/k, proportional to A^{-1}, matches very closely T_{onset} in samples A_{1-3} and B_1 (see Fig. 3.12(e-h) where Δ/k is indicated above each graph). At first sight, our data confirm some earlier reports that linked Δ and T_{onset} [23, 119]. However, we will show hereafter that this rule is only valid is *some* cases and that the openings of the QDs also play a crucial role.

Based on the data presented above, samples B_2 and B_3 have been designed to present a large T_{onset} (small A), and a much larger N than the 4 previous samples. The data for these samples (Fig. 3.13(b)) shows that T_{onset} reaches ~ 5.5 K (in B_3), much larger than in any previous report.[16] Clearly, increasing N results in a larger T_{onset}, so that, now, two parameters (N and Δ), have a similar influence on T_{onset}.

Following these observations, it is natural to plot T_{onset} as a function of the dwell time τ_d, which depends both on Δ and N [Eq. (1.2)]. As emphasized in section 1.1.2, Eq. (1.2) is valid provided that electron trajectories are ergodic and chaotic, and that, ideally, direct trajectories between QPCs are avoided. In some of our QDs, this may not be true (in particular for the last hypothesis, as QPCs are in front of each other in samples B_{1-2} and

[16] In agreement with ref. [41, 84, 130], our data show that $\Delta/k \sim T_{\text{onset}}$ is not generally valid.

A_{1-3}). Nevertheless, we will use Eq. (1.2) for all our QDs, and note that further theoretical work would be needed to obtain a more accurate value of τ_d in each of our samples.

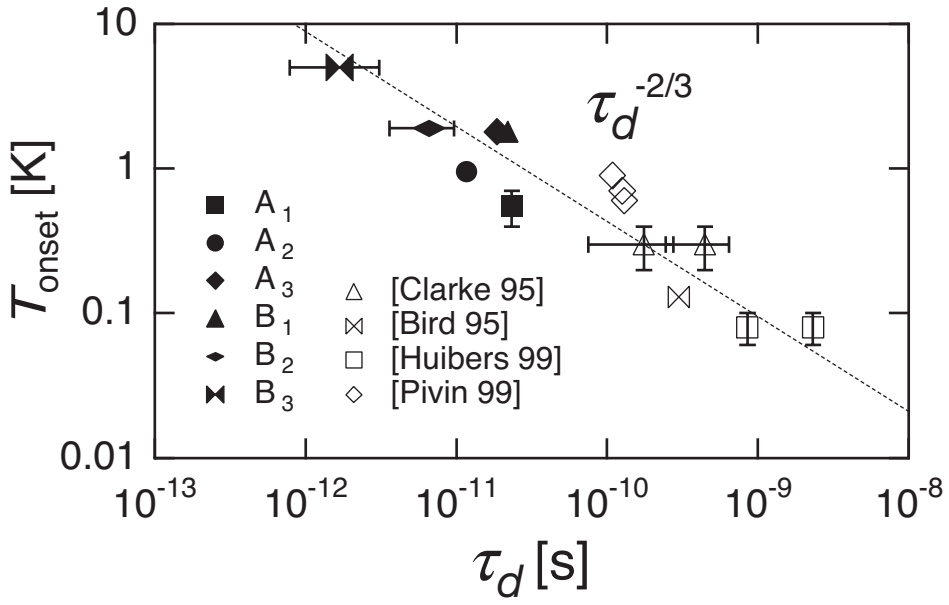

Figure 3.14: $T_{\rm onset}$ vs τ_d in our samples (filled symbols) and in previous works on GaAs QDs (open symbols, see references). The dotted line is a fit to a $\tau_d^{-2/3}$ law (see text).

Fig. 3.14 gathers our data along with $T_{\rm onset}$ vs τ_d from previous works reporting a saturation of τ_ϕ vs T in GaAs QDs [41, 23, 84, 130]. Clearly, $T_{\rm onset}$ rises when τ_d is reduced. More quantitatively, all data condense on a single curve, fitted by $T_{\rm onset} = 10^{-7}\tau_d^{-2/3}$[K]. The very wide range of τ_d over which this power-law is observed is made possible thanks to the complementarity of our data with previous works that all focused on the small-N and large-A regimes, equivalent to a large τ_d. Such a general trend, valid for QDs fabricated from very different substrates and measured in very different conditions, definitely rules out causes of saturation related to the wafer material, or to the measurement system.

Next, we examine whether the relation between $T_{\rm onset}$ and τ_d is "universal", *i.e.*: is it valid for QDs fabricated from any material ? Our measurements on an open bismuth QD [69] presented in chapter 4 give a clue to

answer this question. Based on the calculated $\tau_d \sim 8$ ps in the Bi QD, the fitted-line in Fig. 3.14 gives $T_{\text{onset}} \sim 2.5$ K (± 1 K). The absence of any sign of saturation of τ_ϕ down to 0.3 K in the Bi QD suggests that the observed relation between T_{onset} and τ_d, while relevant for III-V heterostructure QDs, is indeed material- dependent.[17]

In our quest for understanding the saturation of τ_ϕ, Fig. 3.15 is essential as it shows that τ_d is not only the relevant parameter for charting the evolution of T_{onset}, but also for determining τ_ϕ^{sat}. Indeed, we observe that the condition $\tau_\phi^{sat} = \tau_d$ is satisfied over the three orders of magnitude covered by τ_d and τ_ϕ^{sat}. The coherence observed between all experimental results is remarkable knowing that four different methods have been used to obtain τ_ϕ^{sat} shown on Fig. 3.15. However, it is worth noting that all these methods are based on electron interferences occuring *inside* the QD, giving rise to signatures of UCFs or Weak Localization (WL) in its magnetoconductance. Naturally, such interferences occur during the average time spent by electrons inside the QDs, *i.e.* the dwell time. We therefore conclude that the saturation of τ_ϕ in quantum dots originates from the method of determination. Even if the "intrinsic" electron coherence time is larger than τ_d, τ_ϕ extracted from QD magnetoconductance cannot exceed τ_d.[18]

As a consequence of the conclusion drawn above, and since τ_d and the intrinsic electron coherence time τ_ϕ^{int} are independent, we propose to use Matthiessen's rule [13] to derive the effective coherence time in the QD:

$$\frac{1}{\tau_\phi} = \frac{1}{\tau_\phi^{int}} + \frac{1}{\tau_d}. \tag{3.5}$$

The inset to Fig. 3.15 shows that Eq. (3.5), together with the expression for $\tau_\phi^{int} = aT^{-1}$, provides a very good description of the data. This point is remarkable given that a is the only fitting parameter since τ_d is calculated using Eq. 1.2.

We emphasize that Eq. (3.5), valid for QDs, does not exclude a low-T saturation of τ_ϕ^{int}. However, such a saturation could only be evidenced in QDs with a very large τ_d. In this respect, an interesting configuration is the Coulomb blockade regime where τ_d is orders of magnitude larger than in

[17] Further support for this can be found in the dephasing theory. Whatever the dephasing mechanism, τ_ϕ vs T depends on materials parameters such as l_μ and n_s [104]. As we will see below, $\tau_\phi = \tau_d$ when $T = T_{\text{onset}}$, so that τ_d vs T_{onset} is also material-dependent.

[18] In the Bi QD (Bi_1), discussed in next chapter, $\tau_\phi < \tau_d$ at the lowest measurement temperature (0.3 K), which explains why the τ_d-related saturation of τ_ϕ is not observed. Measuring UCFs down to lower temperatures, one could examine if saturation would occur as $\tau_\phi = \tau_d$.

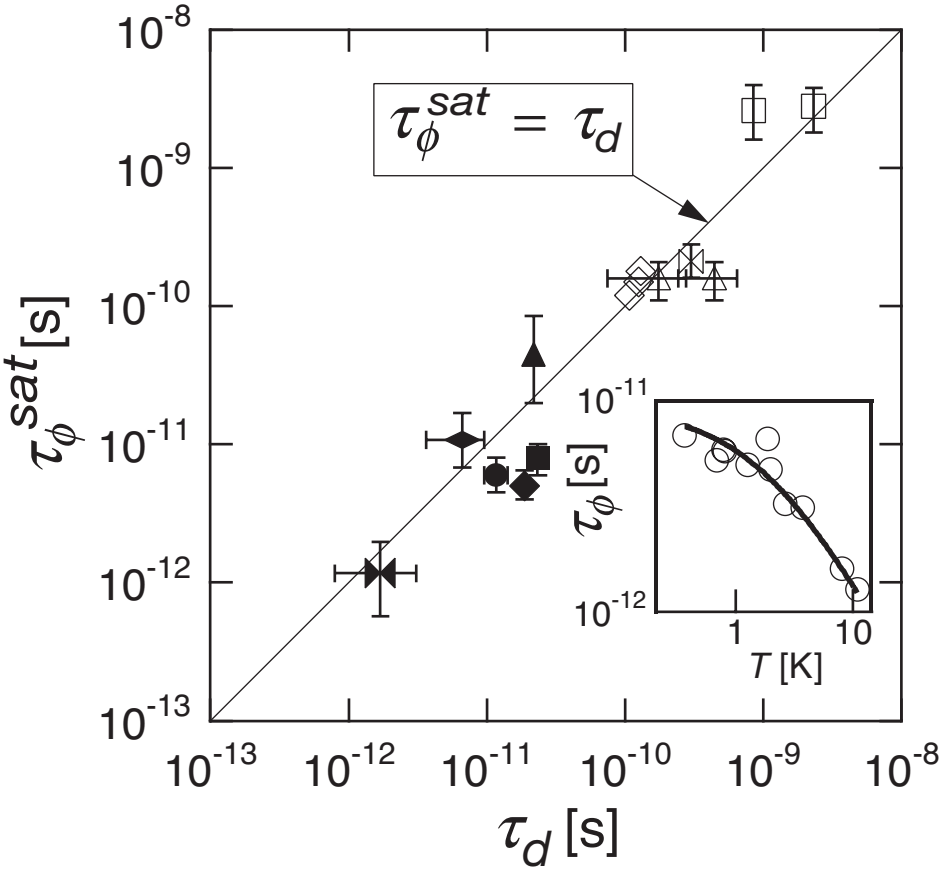

Figure 3.15: τ_ϕ^{sat} vs τ_d (same legend as in Fig. 3.14). The solid line corresponds to $\tau_\phi^{sat} = \tau_d$. Inset: τ_ϕ vs T in sample A_2. The solid line is a fit to Eq. (3.5).

open QDs. Recent experimental and theoretical works [54] focused on the determination of τ_ϕ in such nearly-isolated QDs. No saturation of τ_ϕ vs T was observed, and very large values were found for τ_ϕ, consistent with our data and analysis.

Finally, we point out that we do not rule out some alternative interpretations for our observation ($\tau_\phi^{sat} = \tau_d$). A very recent publication [149] examined (using simulations) the prediction of an exponential suppression of the variance of UCFs and of the WL effect related to the ratios τ_E/τ_ϕ and τ_E/τ_d [5] (see section 1.2.4 for the definition of τ_E). The authors argue that the situation $\tau_\phi = \tau_d$ in quantum dots to the splitting of electron wave packets into partial waves by diffraction at the edge of the point contacts. Alternatively, the mean Lyapunov exponent λ of the cavity may also play a role in the saturation of τ_ϕ: a direct relation between τ_ϕ and λ was recently suggested [93]. In this framework, λ^{-1} would be equal to τ_ϕ^{sat}. This is not in disagreement with our data, as the escape rate from the QD is related to λ (see section 1.1.4). However, establishing a quantitative connection between our results and these theories would require some additional work, in particular to evaluate λ in our QDs.

3.7 Summary

In this chapter, we first reported on very large oscillations of G vs B observed in sample B_1, particularly robust in temperature (visible up to 204 K, at least). We showed that we could associate these oscillations to classical 'focusing' trajectories inside our QD. We calculated the temperature dependence of the focusing mean free path L_f, and find that L_f follows approximately the same temperature dependence as that of the mobility mean free path, although L_f does not seem to saturate at low temperature.

Then, we show how to find the electron coherence time τ_ϕ from the amplitude and correlation function of the UCFs in the range [0.3 K, 20 K]. New methods were employed to extract τ_ϕ, as our samples cover very wide ranges of Δ (so that they violate the condition $\Delta < kT$ at low-T). In our QDs, τ_ϕ exhibits a transition to a T-independent regime below a temperature T_{onset} in the range 0.5 - 5 K.

In B_1, and for $T > T_{\rm onset}$, τ_ϕ vs T was found to obey *quantitatively* the theoretical temperature dependence predicted for 2D disordered systems. Moreover, comparing our data from B_1 to published data from GaAs QDs, we could explain the observed enhancement of τ_ϕ in our samples by means of the same theory. On the other hand, the other QDs showed strong dis-

crepancies with the disordered 2D systems theory. We suggest that these discrepancies come from the population of the second subband, which introduces an additional scattering mechanism deteriorating the electron phase coherence.

Finally, we examined the saturation of the coherence time observed at low temperature. We analyzed both the saturated coherence time τ_ϕ^{sat} and the temperature $T_{\rm onset}$ corresponding to the onset of saturation as a function of sample parameters. We found that a single parameter, the electron dwell time τ_d, governs both $T_{\rm onset}$ and τ_ϕ^{sat} in our samples as well as in all previous works on GaAs QDs. The condition for the occurence of a saturation of τ_ϕ vs T is found to be $\tau_\phi^{sat} = \tau_d$. We argue that this condition is intrinsic to the physics of QDs, in which electron interferences occur only during the average time τ_d spent by electrons inside the cavity. While providing an explanation for the long-standing question of the origin of the low-temperature saturation of τ_ϕ in open quantum dots, we emphasize that our conclusions apply to any confined electronic systems.

The results presented in this chapter have been published in Refs. [64, 65, 66].